



# Numerical simulation of Taylor bubble formation in a microchannel with a converging shape mixing junction



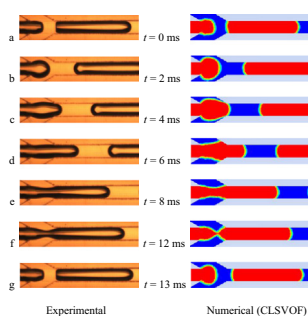
Minhui Dang, Jun Yue, Guangwen Chen\*

Dalian National Laboratory for Clean Energy, Dalian Institute of Chemical Physics, Chinese Academy of Sciences, Dalian 116023, China

## HIGHLIGHTS

- We compared two interface tracking methods of CLSVOF and VOF.
- The CLSVOF method can acquire a more accurate gas–liquid interface.
- The bubble length decreases substantially with the increase of the contact angle.
- End caps of bubbles change from convex to concave with increasing contact angle.

## GRAPHICAL ABSTRACT



## ARTICLE INFO

### Article history:

Received 8 July 2014

Received in revised form 5 October 2014

Accepted 7 October 2014

Available online 12 October 2014

### Keywords:

Microchannel  
Numerical simulation  
Taylor flow  
Bubble  
Contact angle  
Surface tension

## ABSTRACT

The bubble formation in a square microchannel with a converging shape mixing junction has been simulated under Taylor flow using two different interface capturing methods implemented in ANSYS FLUENT (ANSYS Inc., USA): Volume of Fluid (VOF) method, and coupled Level Set and VOF (CLSVOF) method. Compared with VOF method, CLSVOF method can yield a more accurate gas–liquid interface especially at the rupture stage of the emerging bubble and the obtained bubbles are more consistent with the experimental results. The effect of the contact angle ( $\theta$ ), surface tensions ( $\sigma$ ) and liquid viscosity ( $\mu_L$ ) on the Taylor bubble details (i.e., length, volume and shape) has been investigated systematically. For the highest surface tension ( $\sigma = 0.09$  N/m) and the highest liquid viscosity ( $\mu_L = 9.83$  mPa s) investigated, the bubble length decreases substantially with an increase of the contact angle as a result of the combined effect caused by the bubble end shape change from convex to concave and the volume decrease of the liquid film surrounding the bubble body. However, the bubble volume is almost constant regardless of the contact angle, which is mainly caused by the difference in bubble shapes. Both the contact angle and the liquid viscosity have an appreciable influence on the bubble shape whereas the influence of surface tension is minor.

© 2014 Elsevier B.V. All rights reserved.

## 1. Introduction

Over the last two decades, Taylor flow as one common flow pattern encountered during gas–liquid flow in microreactors has become an important field of research due to its excellent trans-

port and reaction properties, such as significant reduction in axial mixing [1], improved radial mixing [2,3], enhanced heat transfer [4], well-defined and tunable interface area available for reaction [5,6]. This flow pattern consists of sequences of an elongated bubble and a liquid slug. The bubble length is usually several times the channel diameter. The liquid slugs are separated by the bubbles and the two adjacent liquid slugs are connected only through a thin film (if present) between the bubble and the channel wall.

\* Corresponding author. Tel.: +86 411 8437 9031; fax: +86 411 8469 1570.

E-mail address: [gwchen@dicp.ac.cn](mailto:gwchen@dicp.ac.cn) (G. Chen).

## Nomenclature

$Ca$	Capillary number defined by ( $Ca = \mu_L j_{TP} / \sigma$ ), dimensionless	<i>Greek letters</i>	
$d_{h\sigma}$	hydraulic diameter, m	$\alpha$	volume fraction
$F_\sigma$	volumetric surface tension force according to CSF method, N/m <sup>3</sup>	$\gamma$	shear rate, s <sup>-1</sup>
$H$	smoothed Heaviside function	$\delta$	smoothed Dirac Delta function
$j_G$	superficial gas velocity, m/s	$\theta$	contact angle, degree
$j_L$	superficial liquid velocity, m/s	$\kappa$	interface curvature
$j_{TP}$	two-phase mixture velocity defined by ( $j_{TP} = j_G + j_L$ ), m/s	$\mu$	viscosity, Pa s
$L_B$	length of Taylor bubble, m	$\rho$	density, kg/m <sup>3</sup>
$L_{inlet}$	length of inlet microchannel, m	$\sigma$	surface tension, N/m
$L_{main}$	length of main microchannel, m	$\varphi$	distance function
$L_S$	length of liquid slug, m		
$p$	pressure, Pa	<i>Subscripts</i>	
$Re$	Reynolds number defined by ( $Re = d_{hTP} \rho_L / \mu_L$ ), dimensionless	$B$	Taylor bubble
$t$	time, s	$e$	expansion step
$\tau$	shear stress defined by ( $\tau = \mu_L \gamma$ ), Pa	film	liquid film
$\vec{u}$	velocity vector, m/s	$G$	gas phase
$V$	volume, m <sup>3</sup>	$L$	liquid phase
$\overline{V}_{film}$	normalized liquid film volume defined by ( $\overline{V}_{film} = V_{film} / V_B$ ), dimensionless	$r$	rupture step
$\vec{x}$	position vector, m	$TP$	two-phase mixture

Microreactors operated under Taylor flow have found potential applications in various chemical processes such as distillation [7], heat exchange [8,9], mixing [10,11], gas absorption [12–17], nanoparticle synthesis [18–21] and homogeneously/heterogeneously catalyzed gas–liquid reactions [5,6,22].

For the manipulation of Taylor flow in microreactors, it is of high importance to enable a precise generation of Taylor bubbles at the microreactor entrance. Many studies [23–32] have revealed that the formation process of Taylor bubbles in microchannels depends on several factors including the inlet mixing junction geometry, the superficial velocities of gas and liquid, surface tension, the wetting properties of the channel wall and the liquid viscosity ( $\mu_L$ ). Garstecki et al. [27] proposed the squeezing mechanism in T-type microfluidic junction geometries that controls the bubble formation at low Capillary numbers (e.g.,  $Ca < 10^{-2}$ ), where the interfacial force is expected to be dominant over the shear stress. Under this regime, the breakup of a Taylor bubble is controlled by the liquid-phase pressure drop across the emerging bubble resulting from its blockage of the liquid flow path. According to this mechanism, they formulated a simple scaling law for the bubble length:

$$\frac{L_B}{w} = 1 + \alpha \frac{j_G}{j_L} \quad (1)$$

where  $L_B$  is the bubble length,  $w$  is the width of the channel,  $j_G$  and  $j_L$  are the superficial velocities for gas and liquid, respectively, and  $\alpha$  is a constant the value of which depends on the geometry of the T-junction. Many researchers [26,33,34] have verified experimentally or numerically the scaling law of Garstecki et al. [27] in the squeezing regime. As a result, the effect of superficial velocities on bubble length has been adequately studied in this regime.

However, the influence of surface tension and the wetting properties of the channel walls on the bubble length in Taylor flow are difficult to be well clarified solely via experiments [35]. The surfactant can be added into the liquid to change the surface tension, yet it always alters the contact angle of the liquid on the wall. Chemical coatings can be applied to channel surfaces to tune the wetting properties of the channel wall, but it is difficult for a quantitative

change of the wetting properties using this method. As observed in our previous experiments [36], the surface tension (changed by the addition of surfactant) seems to have no significant effect on the bubble length. Similar results showing negligible influence of the surface tension on the bubble length produced in the squeezing regime can be also found in the literature [25,27,37,38]. For example, Fu et al. [37] pointed out that the surface tension measured under static conditions could be irrelevant to a fast and dynamical phenomenon for bubble formation. Numerical simulation provides an alternative method to investigate the separate roles of the surface tension and the contact angle during bubble formation in microchannels. One representative work was done by Qian and Lawal [29]. They found that the bubble length slightly increased with an increase of the surface tension and somewhat decreased with the increase of the contact angle of the liquid on the wall from 0° to 90° according to the results of numerical simulation by a Volume of Fluid (VOF) method in a T-type microfluidic junction. This implies that the increase in the surface tension and the contact angle tends to have an opposite influence on the bubble length. In our previous experiments [36], with the decrease of the surface tension by the addition of surfactant to the liquid phase, the contact angle of the liquid on the wall decreased at the same time. This might explain our experimental findings about the observed inappreciable effect of the surface tension on the bubble length. Many other researchers have investigated the effect of the contact angle on Taylor bubble formation by numerical simulation. Some have found that the gas/liquid interface changed from a convex to a concave shape with the increase of the contact angle [28,39]. Some have shown that the bubble and liquid slug lengths decreased slightly until they were almost the same after the liquid became non-wetting [28,29]. Santos and Kawaji [39] investigated the effect of the contact angle, varied from 0° to 140°, on Taylor bubble formation in a microchannel T-junction using computational fluid dynamics (CFD) simulation. They found that the velocity slip occurred due to the stationary liquid at the channel corners for the hydrophilic walls.

In this work, we investigate experimentally and numerically the bubble formation in a microchannel with a converging shape mixing junction. The converging shape mixing geometry is expected to

introduce a smaller pressure drop in the junction than the cross-junction mixing geometry. A further advantage using the covering shape mixing geometry might be that the microchannel wall tends to be preferentially wetted by the liquid at the initial start-up. Thus the mixing junction is expected to facilitate the generation of Taylor bubbles in the downstream microchannel compared with T-junction geometry. An angle of  $60^\circ$  has been selected between the inlet channels. It should be noted that the angle between the inlet channels may affect the bubble formation period and the bubble size. For a larger angle (e.g.,  $90^\circ$  in the case of using a cross-junction) between the inlet channels, it seems that a greater resistance in the liquid phase exists for the bubble formation. Thus, it requires a longer rupture time, resulting in an increase in the bubble length (e.g., see the comparison in Fig. 9 in our previous work [36]). In the existing literature, most authors either paid their attention to the effect of the contact angle at a given surface tension, or investigated the effect of the surface tension at a given contact angle [24,28–30]. As a result, it is difficult to reveal their combined influence on Taylor flow. We extend these earlier studies by performing a detailed numerical investigation on the effect of both the contact angle and surface tension under various gas–liquid flow ratios and liquid viscosities. The main purpose of this work is to further improve our understanding on the formation mechanism of Taylor bubbles in microfluidic geometries in order to achieve more precise control of Taylor flow.

## 2. Experimental

In the experiments, the microchannel with a converging shape mixing junction was fabricated on a polymethyl methacrylate (PMMA) plate, which was sealed with another thin PMMA plate using screw fittings through the punched holes on the peripheries of both plates in order to form a closed microchannel section for fluid passage. Fig. 1 shows the schematic of the microchannel device, where a central inlet microchannel was used for introducing the dispersed gas phase and two side inlet microchannels for introducing the continuous liquid phase. The angle between each side inlet microchannel and the central inlet microchannel is  $30^\circ$ . Taylor flow was generated in the main microchannel. All microchannels have a square cross-section ( $0.6 \text{ mm} \times 0.6 \text{ mm}$ ). The lengths of three inlet microchannels and the main microchannel are 26 mm and 48 mm, respectively.

Gas–liquid Taylor flow was generated in the microchannel device using different fluid-pairs at ambient conditions (about 0.1 MPa,  $20^\circ\text{C}$ ). The experimental setup for Taylor flow regulation

and visualization has been described in our previous work [36]. Here only a brief description is given. Air was used as the gas phase fed into the central inlet microchannel, the flow rate of which was regulated via a mass flow controller. Water, 36 wt% glucose in water, and 45 wt% glucose in water were used as liquids. The liquid flow into each of the two side inlet microchannels was controlled by a separate syringe pump. The Taylor flow pictures in the main microchannel were captured using a high-speed imaging system, from which the Taylor bubble length ( $L_B$ ) could be measured. For each operational condition, experiments were carried out at least thrice and the relative error in  $L_B$  between the measurements was found to be within 5%.

The surface tension values for systems of air–water, air–36 wt% glucose in water, and air–45 wt% glucose in water are 0.0726, 0.0733 and 0.0753 N/m, respectively. The liquid viscosities of water, 36 wt% glucose in water, and 45 wt% glucose in water are 1, 4.42 and 9.83 mPa s, respectively. The contact angle was measured on another machined and flat PMMA plate without microchannel structures, which was found to be  $70^\circ$ ,  $71^\circ$  and  $76^\circ$  for water, 36 wt% glucose in water, and 45 wt% glucose in water on the microchannel wall, respectively. The absolute surface roughness of the machined microchannel is expected to be less than  $1 \mu\text{m}$  [40,41].

## 3. Numerical simulation

### 3.1. Model geometry

A three-dimensional (3D) simulation was performed to investigate Taylor bubble generation in the current microchannel device. The model geometry is a truncated version of the whole device geometry in order to reduce the simulation load, which proved to be sufficient to represent the experimental data. As shown in Fig. 1, the length of the main microchannel in the simulation was set at  $15 d_h$  and the length of each inlet microchannel at  $5 d_h$ .

### 3.2. Governing equations

Different methods are available to capture the interface between two immiscible fluids such as Level Set (LS), Volume of Fluid (VOF), Front Tracking, Phase Field and Lattice Boltzmann [42]. The VOF method is a free-surface tracking technique. It belongs to the class of Eulerian methods which are characterized by a mesh that is either stationary or is moving in a certain prescribed manner to accommodate the evolving shape of the inter-

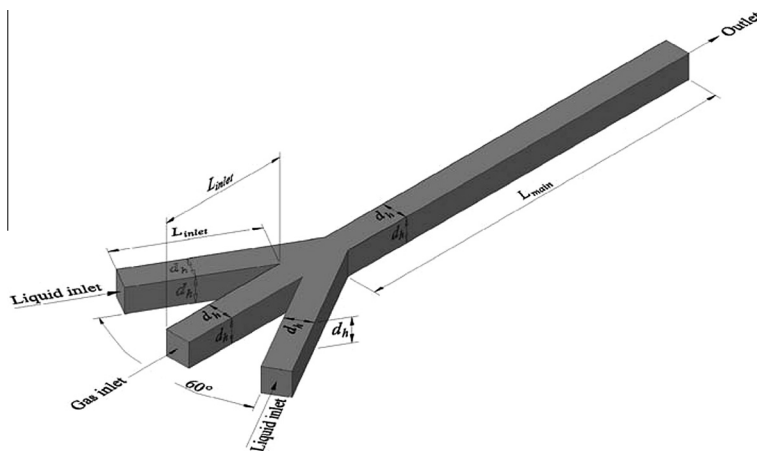


Fig. 1. Schematic diagram of 3D microchannel geometry used in the experiments and simulation.  $L_{inlet} = 5 d_h$ ,  $L_{main} = 15 d_h$  for simulation, and  $L_{inlet} = 43.33 d_h$ ,  $L_{main} = 80 d_h$  for experiments.

face. LS and VOF methods are two of the most widely used methods in the literature, which are popular in simulating two-phase flows with complex interfaces. In the LS method, the interface is tracked and captured by the LS function. The spatial gradients of LS function can be precisely computed due to the continuity and smoothness of LS function. However, the LS method has a weakness in maintaining volume conservation. By contrast, the VOF method is volume-conserved in nature, because it calculates and tracks the volume fraction of a particular phase in each cell rather than the interface itself. The deficiency of the VOF method lies in the computation of its spatial derivatives, as the VOF function is discontinuous across the interface [43]. It is known that spurious velocities could appear due to the improper way the surface tension force is discretized and the surface curvature is approximated.

To overcome the deficiencies of the LS method and the VOF method, a coupled LS and VOF (CLSVOF) approach is provided in ANSYS FLUENT (Release 14.0, ANSYS Inc., USA). In this method, the re-initialization is carried out by using the piecewise linear interface construction (PLIC) geometrical reconstruction. The curvature and interface normal are calculated by the LS function, while the accurate position of the interface is regulated by balancing the volume in each cell in order that the volume fraction calculated from VOF is satisfied. This approach enforces the mass conservation while re-distancing the LS function. The surface tension force and the physical properties of the fluid are calculated in a similar method to the LS method [44].

The commercial CFD package of ANSYS FLUENT (Release 14.0, ANSYS Inc., USA) based on the finite volume method was used in the numerical simulation. The coupled Level Set and Volume of Fluid (CLSVOF) model was implemented in ANSYS FLUENT to capture the gas–liquid interface and the volumetric surface tension in the momentum equation is based on the continuum surface force (CSF). The governing equations for the immiscible, incompressible two phase flows are as follows:

Equation of continuity:

$$\frac{\partial \rho}{\partial t} + \nabla \cdot (\rho \vec{u}) = 0 \quad (2)$$

Equation of momentum:

$$\frac{\partial (\rho \vec{u})}{\partial t} + \nabla \cdot (\rho \vec{u} \vec{u}) = -\nabla p + \nabla \cdot \mu [\nabla \vec{u} + (\nabla \vec{u})^T] + \rho \vec{g} + \vec{F}_\sigma \quad (3)$$

where  $\vec{u}$  is the velocity vector,  $\rho$  is the density,  $\mu$  is the dynamic viscosity of fluid.  $p$  denotes pressure.  $\vec{F}_\sigma$  is the volumetric surface tension force according to CSF method [45].

Equation of VOF function:

$$\frac{\partial \alpha_q}{\partial t} + \vec{u} \cdot \nabla \alpha_q = 0 \quad (4)$$

where  $\alpha_q$  is the volume fraction of  $q$  phase (gas phase or liquid phase).

Equation of Level Set (LS) function:

$$\frac{\partial \phi}{\partial t} + \vec{u} \cdot \nabla \phi = 0 \quad (5)$$

$$\phi(\vec{x}, t) = \begin{cases} d & \text{if } x \text{ in the liquid phase} \\ 0 & \text{if } x \text{ in the interface} \\ -d & \text{if } x \text{ in the gas phase} \end{cases} \quad (6)$$

where  $\phi$  is defined as the distance function,  $\vec{x}$  is the position vector,  $d$  is the shortest distance of a point  $\vec{x}$  from interface at time  $t$ .

The volumetric surface tension  $\vec{F}_\sigma$  based on CSF method:

$$\vec{F}_\sigma = \sigma \kappa(\phi) \delta(\phi) \nabla \phi \quad (7)$$

$$\kappa(\phi) = \nabla \cdot \frac{\nabla \phi}{|\nabla \phi|} \quad (8)$$

$$\delta(\phi) = \begin{cases} 0 & \text{if } |\phi| \geq a \\ \frac{1}{2a} (1 + \cos(\frac{\pi\phi}{a})) & \text{if } |\phi| < a \end{cases} \quad (9)$$

where  $\sigma$  is the surface tension,  $\kappa(\phi)$  is the interface curvature,  $\delta(\phi)$  is the smoothed Dirac Delta function,  $a$  is the interface thickness.

Mixture properties:

$$\rho(\phi) = \rho_G + (\rho_L - \rho_G)H(\phi) \quad (10)$$

$$\mu(\phi) = \mu_G + (\mu_L - \mu_G)H(\phi) \quad (11)$$

$$H(\phi) = \begin{cases} 0 & \text{if } \phi < -a \\ \frac{1}{2} [1 + \frac{\phi}{a} + \frac{1}{\pi} \sin(\frac{\pi\phi}{a})] & \text{if } |\phi| \leq a \\ 1 & \text{if } \phi > a \end{cases} \quad (12)$$

where subscripts  $G$  and  $L$  denote the gas phase and liquid phase, respectively.  $H(\phi)$  is the smoothed Heaviside function.

The flow is treated as incompressible since both the pressure drop (less than 1 kPa) along the microchannel and the superficial gas velocity are small (i.e., in subsonic flow regime). A constant velocity boundary condition was specified at each inlet for the introduction of gas or liquid. The pressure-outlet boundary condition was imposed at the outlet. A static (gauge) pressure is required at the outlet boundary. The value of the specified static pressure is used only while the flow is subsonic. When the flow become locally supersonic, the specified pressure will no longer be used; pressure will be extrapolated from the flow in the interior. All other flow quantities are extrapolated from the interior [43]. In this work, a gauge pressure of 0 Pa for the gas–liquid mixture was applied at the outlet. A no-slip boundary condition was applied at the walls, and the influence of wall adhesion was taken into account by specifying the three-phase contact angle. Rather than imposing the boundary condition at the wall itself, the contact angle at which the fluid is in contact with the wall is used to adjust the surface normal in cells near the wall. This so-called dynamic boundary condition results in the adjustment of the curvature of the surface near the wall, and this curvature is then used to adjust the body force term in the surface tension calculation [43]. At the beginning of the simulation, the entire flow domain was filled with the liquid phase and the initial velocity of the liquid phase in the flow domain was specified to zero.

Air was used as the gas phase. Water and other liquids with different values of viscosity, surface tension, and contact angle were considered. In our simulation, the superficial gas velocity, the superficial liquid velocity, liquid viscosity, surface tension and contact angle ranged from 0.064 to 0.392 m/s, from 0.124 to 0.460 m/s, from 1 to 9.83 mPa s, from 0.01 to 0.09 N/m and from 0° to 150°, respectively.

### 3.3. Solution

The 3D model geometry was meshed using the structured hexahedral elements by the preprocessor GAMBIT and then imported into processor ANSYS FLUENT for calculation. The unsteady term was treated with first-order implicit time stepping. The pressure-implicit with splitting of operators (PISO) algorithm was used for the pressure-velocity coupling and the pressure staggering option (PRESTO) scheme for the pressure term. Second-order upwind scheme was implemented for the momentum equation and the level-set function, and the geometric reconstruction scheme for the volume fraction. The courant number 0.25 for the volume fraction calculation. In the simulations, the time step, the maximum number of iterations per time step, and the relaxation factors were

carefully adjusted to ensure convergence. The simulation results were analyzed by either FLUENT integrated postprocessor or ANSYS CFD-Post.

#### 4. Grid independence and validation of numerical simulation

##### 4.1. Grid independence

The effect of mesh size on the simulation results was investigated by increasing the number of elements from 8550 to 182,280 under a typical operation condition at  $j_G = 0.254$  m/s,  $j_L = 0.124$  m/s,  $\mu_L = 1$  mPa s,  $\sigma = 0.0726$  N/m, and  $\theta = 50^\circ$ , as shown in Fig. 2. Here  $L_B/d_h$ ,  $L_S/d_h$  and  $(L_B + L_S)/d_h$  denote the dimensionless lengths of a bubble, a liquid slug and a unit cell (a Taylor bubble plus a liquid slug), respectively. When the number of elements is over 60,000, the changes in these length parameters are inappreciable. Therefore based on a consideration of the computational time and the accuracy of results, a mesh number of at least 65,100 elements with a grid size of 0.06 mm was mostly used in this work. A much refined mesh with 1,321,200 elements and a grid size of 0.02 mm were used for some extreme cases in order to obtain more physically realistic pictures of bubble formation in the current microchannel, which will be mentioned in our discussion in Section 5.

##### 4.2. Simulation validation with experiments

To examine the validity of our simulation method, a flow visualization experiment was also carried out in the microchannel device (Fig. 1). Fig. 3 shows a comparison between the experimental measurements and numerical simulation using the CLSVOF method on the Taylor bubble formation process during one period under the condition that  $j_G = 0.254$  m/s,  $j_L = 0.124$  m/s,  $\sigma = 0.0726$  N/m,  $\mu_L = 1$  mPa s, and  $\theta = 50^\circ$ . As revealed in our previous work [36], a typical bubble formation process consists of the expansion step (Fig. 3a–c) and the rupture step (Fig. 3d–g). The numerical results are in good agreement with the experimental measurements, allowing the reproduction of the bubble generation details over time. A comparison between the numerical and experimental results on the Taylor bubble length produced at different gas–liquid flow ratios and different liquid viscosities is further depicted in Fig. 4a and b, respectively. The simulated bubble lengths are shown consistent with the experimental data except the existence of a somewhat noticeable difference for a few data points, which could be due to the experimental or simulation

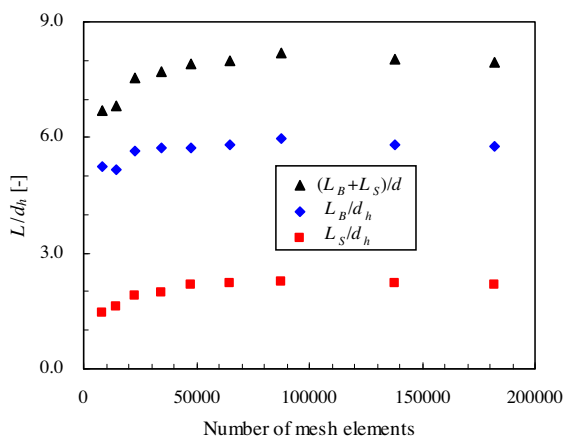


Fig. 2. Grid dependence of the bubble length, liquid slug length and unit cell length.  $j_G = 0.254$  m/s,  $j_L = 0.124$  m/s,  $\mu_L = 1$  mPa s,  $\sigma = 0.0726$  N/m,  $\theta = 50^\circ$ ,  $Ca = 0.005$ ,  $Re = 226.8$ .

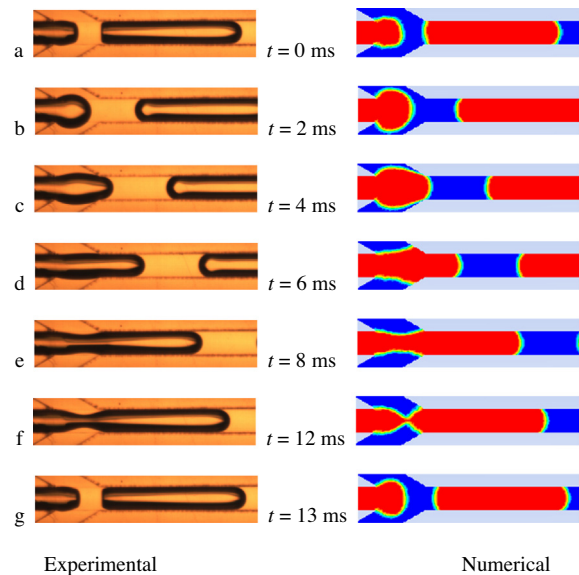


Fig. 3. Comparison of Taylor bubble formation process during one period between the experimental measurements (left images) and the results of numerical simulation with the CLSVOF method (right images). Gas phase: air; liquid phase: water.  $\theta = 50^\circ$ ,  $\sigma = 0.0726$  N/m,  $\mu_L = 1$  mPa s,  $j_G = 0.254$  m/s,  $j_L = 0.124$  m/s,  $Ca = 0.005$ ,  $Re = 226.8$ .

errors. These results corroborate the correctness of our numerical simulation in predicting the behavior of Taylor bubbles in the current microchannel device. It should be noted that the simulation results used to compare with the experimental measurements were obtained at a contact angle of  $50^\circ$  which is a bit lower than the measured contact angle of water on a smooth PMMA plate (i.e.,  $70^\circ$ ). However, the good agreement in the bubble length as shown here suggests that in the experiments the surface roughness of the machined channel wall has lowered the contact angle to some extent, perhaps in combination with other effects such as the effect of microchannel geometry [41].

## 5. Results and discussion

### 5.1. Coupled Level Set and Volume of Fluid (CLSVOF) method

We compared the simulation results by using interface tracking methods of CLSVOF and VOF under the same operational conditions. The same mesh (65,100 elements with a grid size of 0.06 mm) was used for both the CLSVOF and VOF simulations. Fig. 4c shows a quantitative comparison between the predicted bubble lengths from the CLSVOF method and the VOF method. For the CLSVOF method, there is little difference between the simulated lengths of the first and the second bubbles. And they are in good agreement with the experimental results. However, for the VOF method, the difference between the simulated lengths of the first and the second bubbles is much larger, and the simulated lengths also differ a lot from the experimental results. As can be further seen from Fig. 5, the simulation results with the CLSVOF method appear better than that of the VOF method: firstly, the CLSVOF method can acquire a more accurate gas–liquid interface especially at the rupture stage of the bubble; secondly, the bubbles obtained by the CLSVOF method are more uniform in size and are more consistent with the experimental measurements. It may be noted that the computational time with the CLSVOF method is around 1.4 times as long as that with the VOF method for given mesh, time step, and flow case, and the CLSVOF method consumes more memory of computer than the VOF method. If a finer mesh is used with the VOF method, the

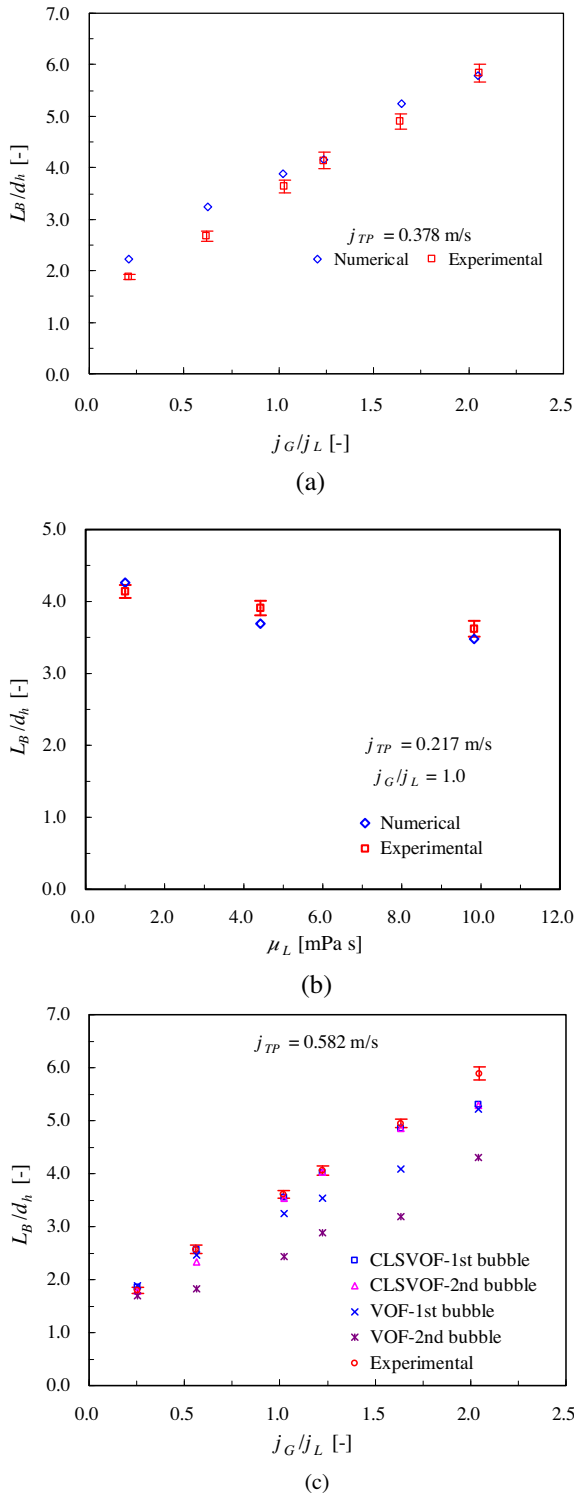


**Fig. 4.** Comparison between the numerical and experimental results on the Taylor bubble length produced under different operational conditions. (a)  $j_{TP} = 0.378$  m/s, gas phase: air; liquid phase: water, simulation results were obtained with the CLSVOF method,  $Ca = 0.005$ ,  $Re = 226.8$ ; (b)  $j_{TP} = 0.217$  m/s, gas phase: air; liquid phase: water ( $\mu_L = 1$  mPa s),  $Ca = 0.003$ ,  $Re = 130.2$ , 36 wt% glucose solution in water ( $\mu_L = 4.42$  mPa s),  $Ca = 0.013$ ,  $Re = 32.4$ , 45 wt% glucose solution in water ( $\mu_L = 9.83$  mPa s),  $Ca = 0.029$ ,  $Re = 15.6$ , simulation results were obtained with the CLSVOF method; (c)  $j_{TP} = 0.582$  m/s, gas phase: air; liquid phase: water, simulation results were obtained with both the CLSVOF method and the VOF method;  $\theta = 50^\circ$ ,  $\sigma = 0.0726$  N/m,  $Ca = 0.008$ ,  $Re = 349.2$ .

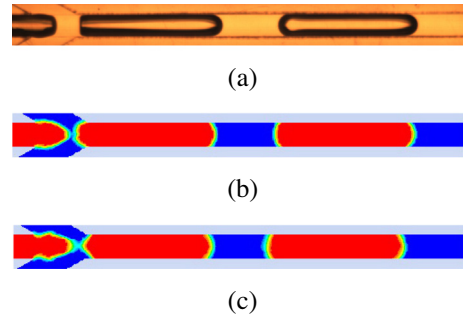


**Fig. 5.** Comparison between the experimental measurements and the simulation results with the interface tracking methods of CLSVOF and VOF. (a) Experiments; (b) CLSVOF method; (c) VOF method. Gas phase: air; liquid phase: water.  $j_G = 0.254$  m/s,  $j_L = 0.124$  m/s,  $\mu_L = 1$  mPa s,  $\sigma = 0.0726$  N/m,  $\theta = 50^\circ$ ,  $Ca = 0.005$ ,  $Re = 226.8$ .

CLSVOF method still performs better than the VOF method for about the same computational time (54 h).

It should be mentioned that the simulated bubble shape in the simulation (cf. Fig. 5b and c) is indeed shown at the center section of the channel. Thus, the liquid film therein is almost not visible in the image due to the close contact of the bubble body with the wall. However, in the experiments (cf. Fig. 5a), the image captured via camera reflects an overall contribution of the whole channel cross section showing the dark shadow caused by the reflection and refraction on curved gas–liquid interface at channel corners. A difference in the radical bubble curvature in the experiments and simulations was also noticed (e.g., by comparing Fig. 5a and b), which might be due to the fact that the wettability of wall in the simulations was considered based on static contact angle while dynamic contact angles are relevant in the experiments. Therefore in this respect, the current simulations need to be further improved.

### 5.2. Effect of the contact angle

We first investigated the effect of the contact angle on the bubble length, bubble volume and pressure drop under various gas–liquid flow ratios, as shown in Fig. 6a–c. At a given contact angle, the bubble length increases (cf. Fig. 6a) with an increase of the gas–liquid flow ratio, which is qualitatively consistent with the existing correlations for the bubble length in the literature (e.g., Eq. (1)) [26,27,34]. In this work, the bubble length was measured as the distance between the nose and the rear of a Taylor bubble in the center line of the microchannel, and it changes little along the main channel. So the axial position in the main channel at which the presented bubble and slug lengths have been measured was near the inlet. For a fixed contact angle, the bubble volume (obtained by a volumetric integral of the gas volume fraction) also increases with the increase of the gas–liquid flow ratio (Fig. 6b).

For a relatively large gas–liquid flow ratio (e.g.,  $j_G/j_L = 2.0$ ), the bubble volume decreases rapidly with the increase of the contact angle from  $30^\circ$  to  $120^\circ$  (Fig. 6b). This is because that the adhesive force on the wall decreases with the increase of the contact angle leading to a reduction in the overall resistance to flow, which is beneficial to the formation of bubbles [27,35]. However, for a relatively small gas–liquid flow ratio, the change of the bubble volume is not as significant as that of the bubble length with the increase of the contact angle. For example, at  $j_G/j_L = 0.5$ , the bubble length decreases substantially with the contact angle being increased from  $30^\circ$  to  $90^\circ$  in contrast to an almost unappreciable decrease

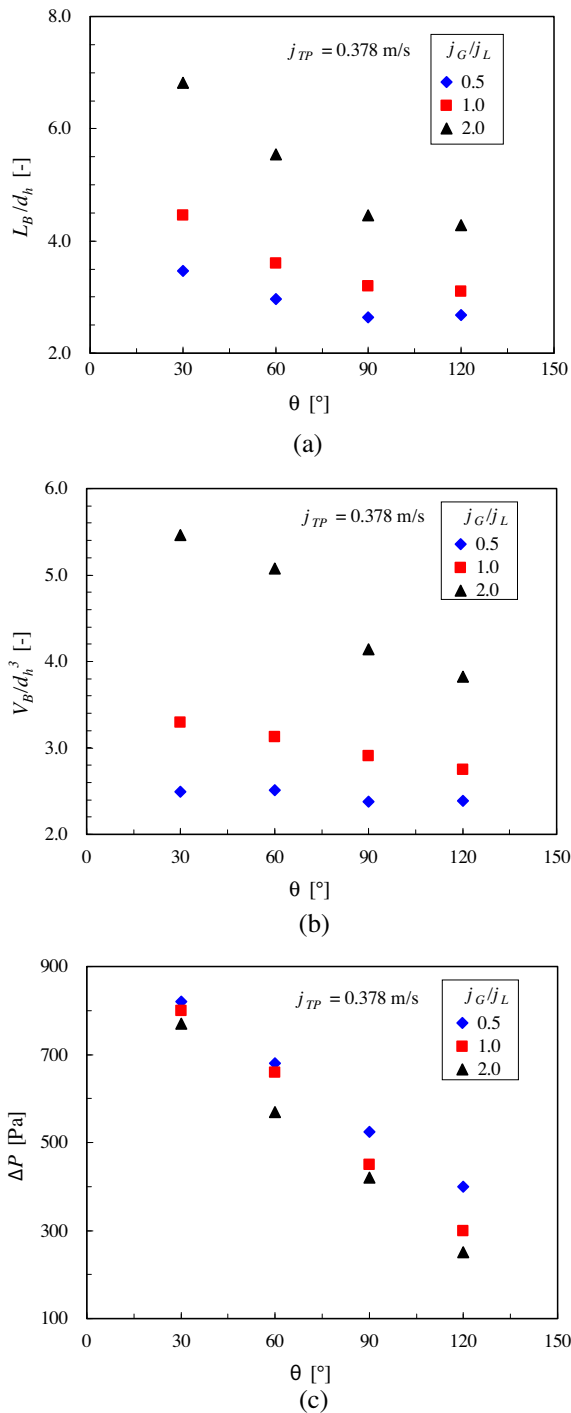


**Fig. 6.** Effect of the contact angle at gas–liquid flow ratios of 0.5, 1.0, 2.0 on (a) bubble length, (b) bubble volume and (c) total pressure drop (measured from the inlet of gas to the outlet of the main microchannel).  $\sigma = 0.0726$  N/m,  $\mu_L = 1$  mPa s,  $j_{TP} = 0.378$  m/s,  $Ca = 0.005$ ,  $Re = 226.8$ .

in the bubble volume. This is mainly caused by the difference in the bubble shape. As shown in Fig. 7, with the increase of the contact angle, both the nose and the rear of a Taylor bubble change from convex shape to concave shape (e.g., see Fig. 7a–d). This shape change of bubble ends will lead to a decrease in the bubble length if one considers a bubble of a given volume in direct contact with the microchannel wall and also indicates that at large contact angles (e.g., at  $120^\circ$ ), there tends to be no liquid film around the bubble body, which is in agreement with the literature observations [46–48]. Moreover, at relatively small contact angles (e.g.,

$\theta = 30^\circ$ , see Fig. 7a, e, i), significant amount of liquid film is present in the four corners of the channel, implying a relatively long bubble under this condition if one considers a bubble of a given volume surrounded by a liquid film along the microchannel wall. Therefore, it is possible that at small gas–liquid flow ratios, the bubble length decreases significantly with the increase in the contact angle although the decrease of the bubble volume remains insignificant. It can be also inferred from Fig. 6a and b that the effect of the contact angle on the bubble length and bubble volume is more pronounced at large gas–liquid flow ratios.

It should be mentioned that the images in Fig. 7d, h and l were obtained in the simulations using the refined mesh (with 1,321,200 elements, grid size 0.02 mm). Otherwise, the bubble residuals would be found around the bubble body, which is due to the false appearance of calculation using the coarse mesh (with 65,100 elements, grid size 0.06 mm). However, the length and volume of the bubble were almost not changed in both cases.

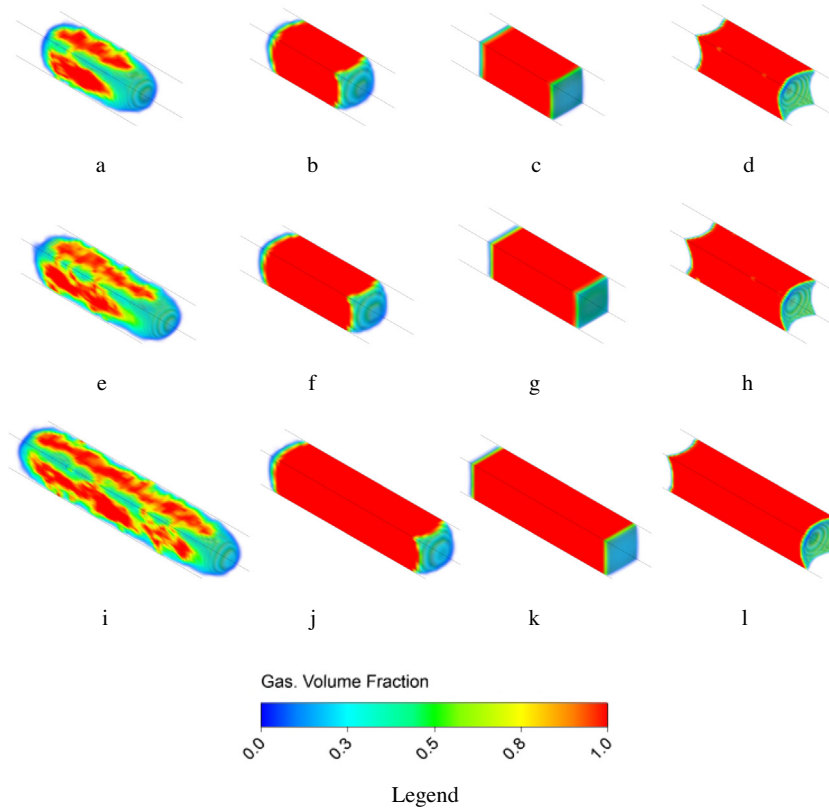
Fig. 6c depicts the total pressure drop under the simulated Taylor flow (measured from the gas inlet to the outlet of the main microchannel) under different gas–liquid flow ratios and contact angles, the two-phase mixture velocity being kept constant. For the same  $j_G/j_L$ , the total pressure drop decreases with an increase in the contact angle, which is mainly because that the pressure drop over bubble end caps is reduced significantly with increasing contact angle due to the shape change gradually from convex to concave (cf. Fig. 7), leading to an overall reduction in the total pressure drop which is a sum of the pressure drop contributions from the liquid slug, the bubble body and its end caps [16]. For a fixed contact angle, the total pressure drop under Taylor flow decreases with the increase of  $j_G/j_L$ . Such decrease in the total pressure drop is mainly caused by a reduction in the pressure drop contribution in the liquid slug given by the fact that the liquid hold up is decreased upon increasing  $j_G/j_L$  (i.e., characterized by shorter liquid slugs and longer bubbles). Remember that here  $j_{TP}$  (i.e., the slug velocity) is fixed, then it is easy to show that the pressure drop contribution in the liquid slug will decrease due to the lower liquid holdup [16].

We further investigated the effect of the contact angle on the flow field under Taylor flow, as revealed in Fig. 8. One preliminary observation is that at small or large contact angles (e.g.,  $\theta = 30^\circ$  or  $120^\circ$ ) where the bubble end caps turn to be in convex or concave shape, the inner circulation inside the bubble is very significant whereas a much less significant inner circulation is seen at contact angle at  $90^\circ$  under which an almost flat bubble end cap is present. A more detailed investigation into such flow behavior will be one main topic of our ongoing work.

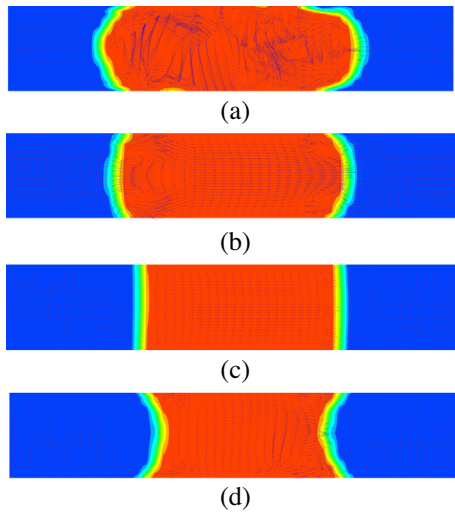
### 5.3. Effect of the surface tension

Fig. 9 depicts the effect of the surface tension under various gas–liquid flow ratios or contact angles on the bubble length (a and b) and the bubble volume (c and d). The bubble length and bubble volume are shown to increase with an increase of the surface tension at  $\theta = 60^\circ$ ,  $j_G/j_L = 0.5$  and 2.0 (Fig. 9a and c) or at  $j_G/j_L = 1.0$ ,  $\theta = 30^\circ$  and or  $120^\circ$  (Fig. 9b and d), which is consistent with the literature results [29]. This is because that the surface tension is the only conservative force which hinders the expansion and the rupture of the emerging bubble [35]. Therefore, a balance of forces is more difficult to reach at higher values of the surface tension, resulting in slower bubble formation and hence larger bubble size.

Compared with the effect of the contact angle, the effect of the surface tension on the bubble length is basically identical to that on the bubble volume (see Fig. 9a and c), which is mainly resulted from the fact that the surface tension has less impact on the shape of the bubble and the liquid film around the bubble body than the contact angle (see Fig. 10).



**Fig. 7.** Effect of the contact angle on the bubble shape. The red color, blue color and the intermediate color represent the gas phase, the liquid phase and the gas–liquid interface, respectively. Lines in the figures represent the channel contour.  $\sigma = 0.0726$  N/m,  $\mu_L = 1$  mPa s,  $j_{TP} = 0.378$  m/s,  $Ca = 0.005$ ,  $Re = 226.8$ .  $j_c/j_L = 0.5$  for (a)  $\theta = 30^\circ$ ; (b)  $\theta = 60^\circ$ ; (c)  $\theta = 90^\circ$ ; (d)  $\theta = 120^\circ$ ;  $j_c/j_L = 1.0$  for (e)  $\theta = 30^\circ$ ; (f)  $\theta = 60^\circ$ ; (g)  $\theta = 90^\circ$ ; (h)  $\theta = 120^\circ$ ;  $j_c/j_L = 2.0$  for (i)  $\theta = 30^\circ$ ; (j)  $\theta = 60^\circ$ ; (k)  $\theta = 90^\circ$ ; (l)  $\theta = 120^\circ$ . (For interpretation of the references to color in this figure legend, the reader is referred to the web version of this article.)



**Fig. 8.** Vector of velocity superimposed on contours of gas volume fraction (red). The red color, blue color and the intermediate color represent the gas phase, the liquid phase and the gas–liquid interface, respectively. (a)  $\theta = 30^\circ$ ; (b)  $\theta = 60^\circ$ ; (c)  $\theta = 90^\circ$ ; (d)  $\theta = 120^\circ$ .  $\sigma = 0.0726$  N/m,  $\mu_L = 1$  mPa s,  $j_c/j_L = 0.5$ ,  $j_{TP} = 0.378$  m/s,  $Ca = 0.005$ ,  $Re = 226.8$ . (For interpretation of the references to color in this figure legend, the reader is referred to the web version of this article.)

5.4. Effect of the liquid viscosity

Fig. 11 presents the results showing the effect of the liquid viscosity on the bubble size. It is firstly seen that with an increase of

the liquid viscosity from 1 to 9.83 mPa s, the effect of the contact angle on the bubble volume is different (cf. Fig. 11b and d). At a comparatively low liquid viscosity (e.g.,  $\mu_L = 1$  mPa s), the bubble volume decreases with the increase of the contact angle. However, for comparatively high liquid viscosity (e.g.,  $\mu_L = 9.83$  mPa s), the bubble volume does not change significantly with the increase of the contact angle. This is because that when the liquid viscosity is high, the influence of adhesion force is less obvious compared to the shear force during the bubble break-up. By comparing Fig. 11c and d, one can further see that at a relatively high liquid viscosity (e.g.,  $\mu_L = 9.83$  mPa s), the bubble length decreases substantially with the increase of the contact angle (Fig. 11c) in contrast to an almost constant bubble volume at different contact angles (Fig. 11d). As we have discussed before, the bubble (albeit insignificant change in its volume) can experience a significant decrease in its length with increasing contact angle as a result of the combined effect caused by the end shape change from convex to concave and the decrease of the liquid film volume around the bubble. This combined effect is also present at the present condition of  $\mu_L = 9.83$  mPa s. As shown in Fig. 12, with the increase of the contact angle, both the nose and the rear of Taylor bubble tend to change from a convex shape to a concave shape. Moreover, as shown in Fig. 13, the normalized liquid film volume surrounding the bubble body (designated as  $\bar{V}_{film}$ , being calculated as  $\bar{V}_{film} = V_{film}/V_B$ ) as measured from the simulation results decreases with the increase of the contact angle. This explains the observed difference in the variation of the bubble length with the contact angle from that of the bubble volume at  $\mu_L = 9.83$  mPa s.

By comparing Fig. 11a and c, one can see that for a relatively high liquid viscosity of  $\mu_L = 9.83$  mPa s, the bubble length varies insignificantly with the increasing contact angle at  $\sigma = 0.03$  N/m

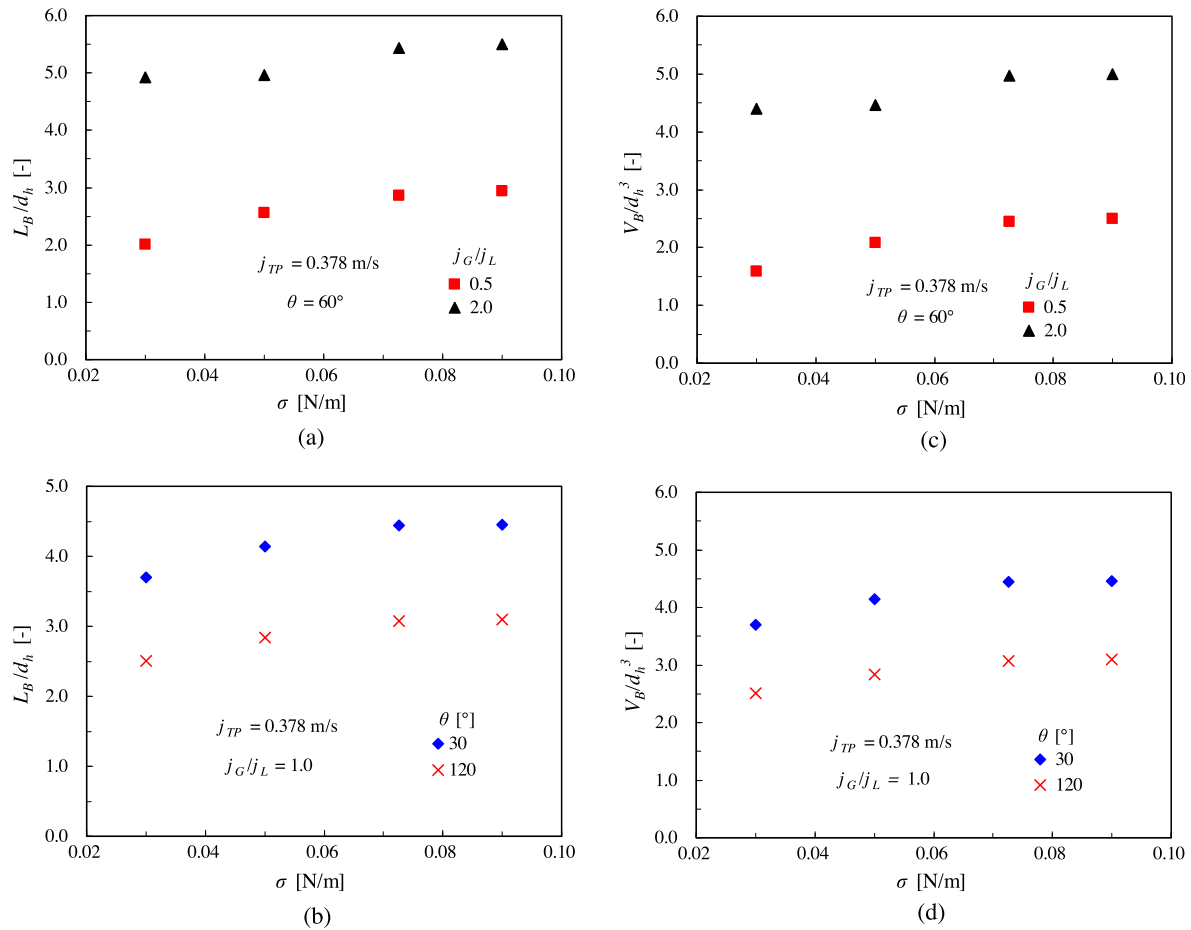


**Fig. 9.** Effect of the surface tension under various gas–liquid flow ratios or contact angles on the bubble length (a and b) and the bubble volume (c and d).  $\mu_L = 1$  mPa s,  $j_{TP} = 0.378$  m/s,  $Re = 226.8$ .

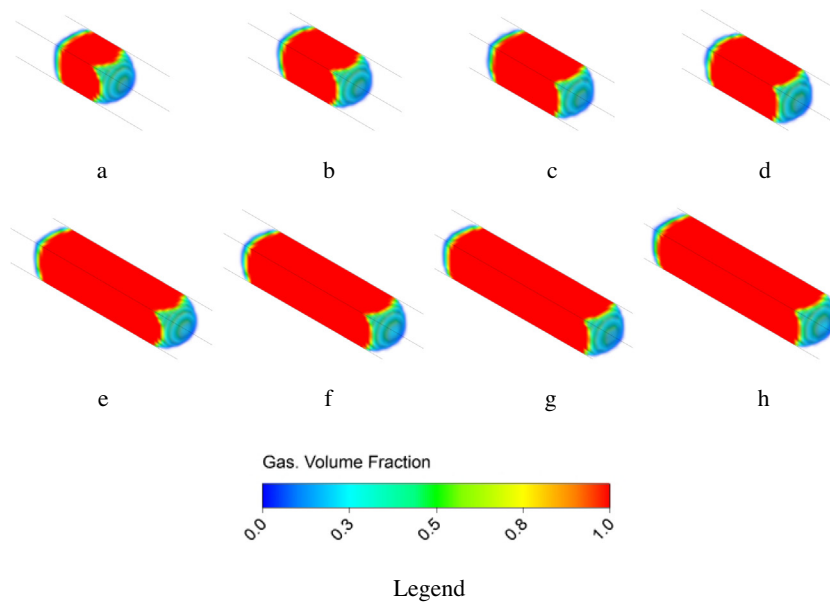


**Fig. 10.** Effect of the surface tension on the bubble shape. Lines in the figures represent the channel contour.  $\theta = 60^\circ$ ,  $\mu_L = 1$  mPa s,  $j_{TP} = 0.378$  m/s,  $Re = 226.8$ .  $j_G/j_L = 0.5$  for (a)  $\sigma = 0.03$  N/m,  $Ca = 0.013$ ; (b)  $\sigma = 0.05$  N/m,  $Ca = 0.008$ ; (c)  $\sigma = 0.0726$  N/m,  $Ca = 0.005$ ; (d)  $\sigma = 0.09$  N/m,  $Ca = 0.004$ ;  $j_G/j_L = 2.0$  for (e)  $\sigma = 0.03$  N/m,  $Ca = 0.013$ ; (f)  $\sigma = 0.05$  N/m,  $Ca = 0.008$ ; (g)  $\sigma = 0.0726$  N/m,  $Ca = 0.005$ ; (h)  $\sigma = 0.09$  N/m,  $Ca = 0.004$ .

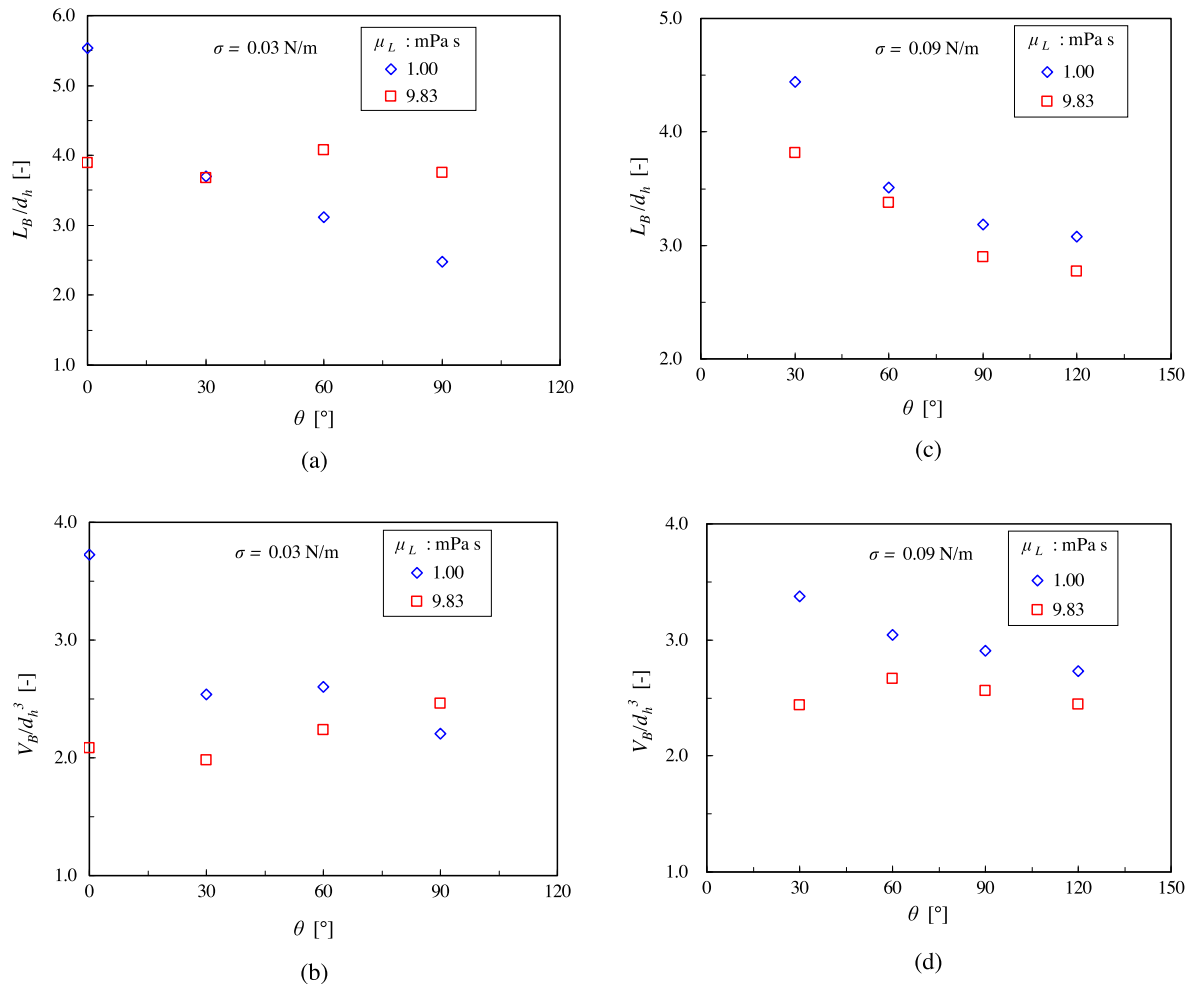


**Fig. 11.** Effect of the liquid viscosity on (a) the bubble length at  $\sigma = 0.03$  N/m, (b) the bubble volume at  $\sigma = 0.03$  N/m, (c) the bubble length at  $\sigma = 0.09$  N/m and (d) the bubble volume at  $\sigma = 0.09$  N/m.  $j_C = 0.189$  m/s,  $j_L = 0.189$  m/s.

whereas it exhibits a significant decrease with increasing contact angle at  $\sigma = 0.09$  N/m. As explained before, two factors contribute to the decrease of the bubble length with increasing contact angle: the change of bubble end shape from convex to concave; and the decrease of the normalized liquid film volume surrounding the bubble body. The latter effect, as shown in Fig. 13, is more pronounced at  $\sigma = 0.09$  N/m compared with that at  $\sigma = 0.03$  N/m for  $\mu_L = 9.83$  mPa s. This would therefore lead to a more noticeable decrease of the bubble length with the contact angle at  $\sigma = 0.09$  N/m for  $\mu_L = 9.83$  mPa s. In contrast, the bubble length shows a similar decrease with increasing contact angle for  $\mu_L = 1$  mPa s as  $\sigma$  is increased from 0.03 to 0.09 N/m, as shown in Fig. 11a and c. This is explained by the comparable extent of decrease in the normalized liquid film volume with increasing contact angle for both  $\sigma$  values (cf. Fig. 13).

## 6. Conclusions

The bubble formation in a square microchannel with a converging shape mixing junction has been investigated under gas–liquid Taylor flow using a geometric coupled Level Set and VOF (CLSVOF) method implemented in ANSYS FLUENT. The effect of the gas–liquid flow ratio, contact angle, surface tension and liquid viscosity on the bubble length and the bubble volume has been studied. Based on the results of this study, the following conclusions can be drawn:

- (1) Compared with the Volume of Fluid (VOF) method, the CLSVOF method can acquire a more accurate gas–liquid interface especially at the rupture stage of the bubble and the bubbles obtained are more consistent with the experimental results.
- (2) For a relatively large gas–liquid flow ratio (e.g., at  $j_C/j_L = 2.0$ ), both the bubble volume and bubble length decreases significantly with the increase of the contact angle from 30° to 120°. At a relatively small gas–liquid flow ratio (e.g., at  $j_C/j_L = 0.3$ ), the decrease of the bubble volume is not as significant as that of the bubble length with increasing contact angle. The bubble volume and bubble length increase with an increase of the surface tension. At a comparatively low liquid viscosity (e.g.,  $\mu_L = 1$  mPa s), the bubble volume decreases upon increasing the contact angle. However, at comparatively high liquid viscosity (e.g.,  $\mu_L = 9.83$  mPa s), the bubble volume does not change significantly with increasing contact angle.
- (3) With the increase of the contact angle, both the nose and the rear of a Taylor bubble change from a convex shape to a concave shape. The volume of liquid film surrounding the bubble body decreases with the increase of the contact angle or surface tension.

Detailed understanding of the important factors influencing Taylor bubble formation in microfluidic geometries is necessary, allowing for a rational design and operation of microfluidic devices

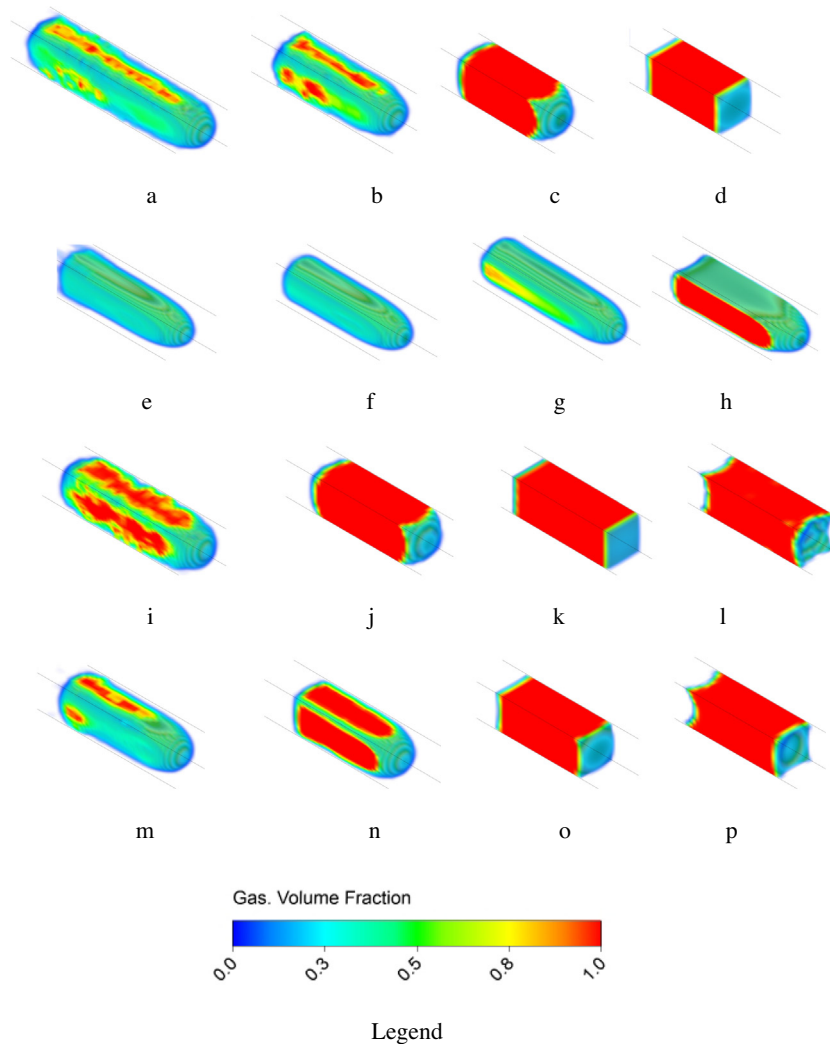


**Fig. 12.** Effect of the liquid viscosity, contact angle and surface tension on the bubble shape.  $j_G = 0.189$  m/s,  $j_L = 0.189$  m/s.  $\sigma = 0.03$  N/m and  $\mu_L = 1$  mPa s,  $Ca = 0.013$ ,  $Re = 226.8$  for (a)  $\theta = 0^\circ$ ; (b)  $\theta = 30^\circ$ ; (c)  $\theta = 60^\circ$ ; (d)  $\theta = 90^\circ$ ;  $\sigma = 0.03$  N/m and  $\mu_L = 9.83$  mPa s,  $Ca = 0.005$ ,  $Re = 23.1$  for (e)  $\theta = 0^\circ$ ; (f)  $\theta = 30^\circ$ ; (g)  $\theta = 60^\circ$ ; (h)  $\theta = 90^\circ$ ;  $\sigma = 0.09$  N/m and  $\mu_L = 1$  mPa s,  $Ca = 0.004$ ,  $Re = 226.8$  for (i)  $\theta = 30^\circ$ ; (j)  $\theta = 60^\circ$ ; (k)  $\theta = 90^\circ$ ; (l)  $\theta = 120^\circ$ ;  $\sigma = 0.09$  N/m and  $\mu_L = 9.83$  mPa s,  $Ca = 0.04$ ,  $Re = 23.1$  for (m)  $\theta = 30^\circ$ ; (n)  $\theta = 60^\circ$ ; (o)  $\theta = 90^\circ$ ; (p)  $\theta = 120^\circ$ .

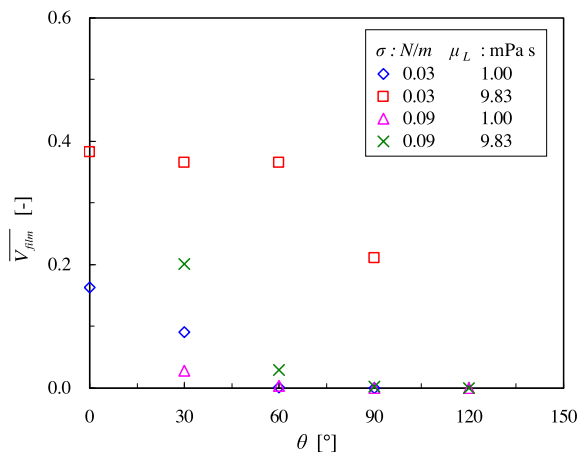


**Fig. 13.** Effect of the liquid viscosity, contact angle and surface tension on the normalized liquid film volume surrounding the bubble body.  $j_G = 0.189$  m/s,  $j_L = 0.189$  m/s.

relying on the manipulation of Taylor flow in diversified applications. Although elaborate experimental characterization remains as the most effective approach to clarify this issue, numerical

simulation is capable of providing further insights usually not accessible through experiments only. The present simulation work represents such an attempt and the future work would be in the real-time monitoring of the surface tension, shear stress and inertial forces during the bubble formation by numerical simulation. It may be mentioned that the meshes used in the current simulation are still coarse in terms of defining a very precise and accurate gas-liquid interface and thus there is an inevitable presence of numerical diffusion. Therefore, the physical transport mechanisms at the interface cannot be revealed in full details although such meshes are sufficient in revealing the behavior of the average properties such as the bubble length and volume as studied in this work.

#### Acknowledgments

The work was financially supported by research grants from the National Natural Science Foundation of China (NSFC) (Nos. 21225627 and 91334201), and the framework of the Sino-French project MIGALI via the NSFC (No. 20911130358).

#### References

- [1] T.C. Thulasidas, M.A. Abraham, R.L. Cerro, Dispersion during bubble-train flow in capillaries, *Chem. Eng. Sci.* 54 (1999) 61–76.

- [2] G. Berčić, A. Pintar, The role of gas bubbles and liquid slug lengths on mass transport in the Taylor flow through capillaries, *Chem. Eng. Sci.* 52 (1997) 3709–3719.
- [3] J.M. van Baten, R. Krishna, CFD simulations of wall mass transfer for Taylor flow in circular capillaries, *Chem. Eng. Sci.* 60 (2005) 1117–1126.
- [4] Y.S. Muzychka, E.J. Walsh, P. Walsh, Heat Transfer Enhancement Using Laminar Gas–Liquid Segmented Plug Flows, *J. Heat Transfer Trans. Asme* 133 (2011).
- [5] J.J.W. Bakker, M.M.P. Zieverink, R. Reintjens, F. Kapteijn, J.A. Moulijn, M.T. Kreutzer, Heterogeneously catalyzed continuous-flow hydrogenation using segmented flow in capillary columns, *ChemCatChem* 3 (2011) 1155–1157.
- [6] T. Yasukawa, W. Ninomiya, K. Ooyachi, N. Aoki, K. Mae, Enhanced production of ethyl pyruvate using gas–liquid slug flow in microchannel, *Chem. Eng. J.* 167 (2011) 527–530.
- [7] R.L. Hartman, H.R. Sahoo, B.C. Yen, K.F. Jensen, Distillation in microchemical systems using capillary forces and segmented flow, *Lab Chip* 9 (2009) 1843–1849.
- [8] R. Gupta, D.F. Fletcher, B.S. Haynes, CFD modelling of flow and heat transfer in the Taylor flow regime, *Chem. Eng. Sci.* 65 (2010) 2094–2107.
- [9] S.S.Y. Leung, Y. Liu, D.F. Fletcher, B.S. Haynes, Heat transfer in well-characterised Taylor flow, *Chem. Eng. Sci.* 65 (2010) 6379–6388.
- [10] A. Günther, M. Jhunjhunwala, M. Thalmann, M.A. Schmidt, K.F. Jensen, Micromixing of miscible liquids in segmented gas–liquid flow, *Langmuir* 21 (2005) 1547–1555.
- [11] P. Garstecki, M.A. Fischbach, G.M. Whitesides, Design for mixing using bubbles in branched microfluidic channels, *Appl. Phys. Lett.* 86 (2005) 244108.
- [12] G. Chen, J. Yue, Q. Yuan, Gas–liquid microreaction technology: recent developments and future challenges, *Chin. J. Chem. Eng.* 16 (2008) 663–669.
- [13] C. Ye, G. Chen, Q. Yuan, Process characteristics of CO<sub>2</sub> absorption by aqueous monoethanolamine in a microchannel reactor, *Chin. J. Chem. Eng.* 20 (2012) 111–119.
- [14] C. Ye, M. Dang, C. Yao, G. Chen, Q. Yuan, Process analysis on CO<sub>2</sub> absorption by monoethanolamine solutions in microchannel reactors, *Chem. Eng. J.* 225 (2013) 120–127.
- [15] J. Yue, G. Chen, Q. Yuan, L. Luo, Y. Gonthier, Hydrodynamics and mass transfer characteristics in gas–liquid flow through a rectangular microchannel, *Chem. Eng. Sci.* 62 (2007) 2096–2108.
- [16] J. Yue, L. Luo, Y. Gonthier, G. Chen, Q. Yuan, An experimental study of air–water Taylor flow and mass transfer inside square microchannels, *Chem. Eng. Sci.* 64 (2009) 3697–3708.
- [17] J. Yue, R. Boichot, L. Luo, Y. Gonthier, G. Chen, Q. Yuan, Flow distribution and mass transfer in a parallel microchannel contactor integrated with structural distributors, *AIChE J.* 56 (2010) 298–317.
- [18] V.S. Cabeza, S. Kuhn, A.A. Kulkarni, K.F. Jensen, Size-controlled flow synthesis of gold nanoparticles using a segmented flow microfluidic platform, *Langmuir* 28 (2012) 7007–7013.
- [19] A. Günther, S.A. Khan, M. Thalmann, F. Trachsel, K.F. Jensen, Transport and reaction in microscale segmented gas–liquid flow, *Lab Chip* 4 (2004) 278–286.
- [20] S.A. Khan, A. Günther, M.A. Schmidt, K.F. Jensen, Microfluidic synthesis of colloidal silica, *Langmuir* 20 (2004) 8604–8611.
- [21] B.K.H. Yen, A. Günther, M.A. Schmidt, K.F. Jensen, M.G. Bawendi, A microfabricated gas–liquid segmented flow reactor for high-temperature synthesis: the case of CdSe quantum dots, *Angew. Chem. Int. Ed.* 44 (2005) 5447–5451.
- [22] S.R.A. de Loos, J. van der Schaaf, M. de Croon, T.A. Nijhuis, J.C. Schouten, Heterogeneous catalysis in a microchannel using a layer of carbon nanofibers on the channel wall, *Chem. Eng. J.* 179 (2012) 242–252.
- [23] L. Dai, W. Cai, F. Xin, Numerical study on bubble formation of a gas–liquid flow in a T-junction microchannel, *Chem. Eng. Technol.* 32 (2009) 1984–1991.
- [24] N. Dietrich, S. Poncin, N. Midoux, H.Z. Li, Bubble formation dynamics in various flow-focusing microdevices, *Langmuir* 24 (2008) 13904–13911.
- [25] T. Fu, D. Funfschilling, Y. Ma, H. Li, Scaling the formation of slug bubbles in microfluidic flow-focusing devices, *Microfluid. Nanofluid.* 8 (2010) 467–475.
- [26] T. Fu, Y. Ma, D. Funfschilling, C. Zhu, H.Z. Li, Squeezing-to-dripping transition for bubble formation in a microfluidic T-junction, *Chem. Eng. Sci.* 65 (2010) 3739–3748.
- [27] P. Garstecki, M.J. Fuerstman, H.A. Stone, G.M. Whitesides, Formation of droplets and bubbles in a microfluidic T-junction – scaling and mechanism of break-up, *Lab Chip* 6 (2006) 437–446.
- [28] V. Kumar, S. Vashisth, Y. Hoarau, K.D.P. Nigam, Slug flow in curved microreactors: hydrodynamic study, *Chem. Eng. Sci.* 62 (2007) 7494–7504.
- [29] D. Qian, A. Lawal, Numerical study on gas and liquid slugs for Taylor flow in a T-junction microchannel, *Chem. Eng. Sci.* 61 (2006) 7609–7625.
- [30] N. Shao, W. Salman, A. Gavriilidis, P. Angeli, CFD simulations of the effect of inlet conditions on Taylor flow formation, *Int. J. Heat Fluid Flow* 29 (2008) 1603–1611.
- [31] J. Tan, S.W. Li, K. Wang, G.S. Luo, Gas–liquid flow in T-junction microfluidic devices with a new perpendicular rupturing flow route, *Chem. Eng. J.* 146 (2009) 428–433.
- [32] J. Yue, L. Luo, Y. Gonthier, G. Chen, Q. Yuan, An experimental investigation of gas–liquid two-phase flow in single microchannel contactors, *Chem. Eng. Sci.* 63 (2008) 4189–4202.
- [33] M. De Menech, P. Garstecki, F. Jousse, H.A. Stone, Transition from squeezing to dripping in a microfluidic T-shaped junction, *J. Fluid Mech.* 595 (2008) 141–161.
- [34] V. van Steijn, M.T. Kreutzer, C.R. Kleijn, Mu-PIV study of the formation of segmented flow in microfluidic T-junctions, *Chem. Eng. Sci.* 62 (2007) 7505–7514.
- [35] S. Bashir, J.M. Rees, W.B. Zimmerman, Simulations of microfluidic droplet formation using the two-phase level set method, *Chem. Eng. Sci.* 66 (2011) 4733–4741.
- [36] M. Dang, J. Yue, G. Chen, Q. Yuan, Formation characteristics of Taylor bubbles in a microchannel with a converging shape mixing junction, *Chem. Eng. J.* 223 (2013) 99–109.
- [37] T. Fu, Y. Ma, D. Funfschilling, H.Z. Li, Bubble formation and breakup mechanism in a microfluidic flow-focusing device, *Chem. Eng. Sci.* 64 (2009) 2392–2400.
- [38] S. Laborie, C. Cabassud, L. Durand-Bourlier, J.M. Lainé, Characterisation of gas–liquid two-phase flow inside capillaries, *Chem. Eng. Sci.* 54 (1999) 5723–5735.
- [39] R.M. Santos, M. Kawaji, Developments on wetting effects in microfluidic slug flow, *Chem. Eng. Commun.* 199 (2012) 1626–1641.
- [40] P.-C. Chen, C.-W. Pan, W.-C. Lee, K.-M. Li, An experimental study of micromilling parameters to manufacture microchannels on a PMMA substrate, *Int. J. Adv. Manuf. Technol.* 71 (2014) 1623–1630.
- [41] K. Hecht, F. Messerschmidt, P. Pfeifer, R. Dittmeyer, B. Kraushaar-Czarnetzki, S. Hecht, Surface roughness of machined microchannels and its effect on multiphase boundary conditions, *Chem. Eng. J.* 227 (2013) 2–12.
- [42] M. Wörner, Numerical modeling of multiphase flows in microfluidics and micro process engineering: a review of methods and applications, *Microfluid. Nanofluid.* 12 (2012) 841–886.
- [43] ANSYS, ANSYS FLUENT Theory Guide, ANSYS FLUENT Release 14.0 ed., ANSYS Inc., Canonsburg, PA 15317, USA, 2011.
- [44] A. Albadawi, D.B. Donoghue, A.J. Robinson, D.B. Murray, Y.M.C. Delauré, On the analysis of bubble growth and detachment at low Capillary and Bond numbers using Volume of Fluid and Level Set methods, *Chem. Eng. Sci.* 90 (2013) 77–91.
- [45] J.U. Brackbill, D.B. Kothe, C. Zemach, A continuum method for modeling surface tension, *J. Comput. Phys.* 100 (1992) 335–354.
- [46] T. Cubaud, U. Ulmanella, C.-M. Ho, Two-phase flow in microchannels with surface modifications, *Fluid Dyn. Res.* 38 (2006) 772–786.
- [47] S.A. Kazemi Oskoeei, D. Sinton, Partial wetting gas–liquid segmented flow microreactor, *Lab Chip* 10 (2010) 1732–1734.
- [48] J. Yue, F.H. Falke, J.C. Schouten, T.A. Nijhuis, Microreactors with integrated UV/Vis spectroscopic detection for online process analysis under segmented flow, *Lab Chip* 13 (2013) 4855–4863.